Time-Domain Modeling of Constant Phase Elements for Simulation of Lithium Battery Behavior

Chun-Sing Cheng, *Student Member, IEEE*, Henry Shu-Hung Chung, *Fellow, IEEE*, Ricky Wing-Hong Lau, *Senior Member, IEEE*, and Kelvin Yi-Wen Hong

***Abstract*—A computational model for simulating the time-domain response of lithium batteries under arbitrary charging and discharging profiles is presented. The methodology is based on first formulating a mathematical model that describes the time-domain voltage–current characteristics of constant phase elements (CPEs), and then uses multiple series-connected CPEs, as well as charge transfer resistances, output resistances, and inductances, to form the computational model. The criteria for ensuring the stability of the computational model will be derived. The validity of the computational model is confirmed by comparing the simulation results of a model consisting of three series-connected CPEs with the measurement results of six SANYO 18650, 3300-mAh, 3.7-V rechargeable Li-ion batteries under controlled charging and discharging profiles. Finally, the accuracy of the computational model will be compared to the accuracy of the models using different orders of parallel resistor–capacitor networks.**

***Index Terms*—Constant phase elements (CPE), computational modeling, energy storage devices, lithium batteries.**

I. Introduction

ELECTROCHEMICAL batteries are becoming increasingly important in smart city development and fourth industrial revolution (Industry 4.0) [1], [2], as they are used to buffer fluctuations in local energy generation and demand. It is thus crucial to understand battery condition, provide operators with performance predictions, and maximize battery life with sophisticated battery management systems. As the variables that can be accessed are only battery voltage, battery current, and temperature, it is sometimes necessary to rely on the use of battery models to estimate intrinsic conditions and predict electrical characteristics. Battery models are available in both offline and online versions. Generally, offline models are used for system design and analysis, while online models

Manuscript received June 3, 2018; revised September 25, 2018; accepted October 30, 2018. Date of publication November 13, 2018; date of current version May 22, 2019. This work was supported in part by a Grant from the Innovation and Technology Fund of the Hong Kong Special Administrative Region, China, under Project #ITS/277/14 and in part by a Grant from the City University of Hong Kong, under Project #7004841. This paper was presented at the IEEE Applied Power Electronics Conference and Exposition, Tampa, FL, USA, March 26–30, 2017. Recommended for publication by Associate Editor O. Trescases. *(Corresponding author: Henry Shu-Hung Chung.)*

The authors are with the Centre for Smart Energy Conversion and Utilization Research and the Department of Electronic Engineering, City University of Hong Kong, Kowloon, Hong Kong (e-mail:

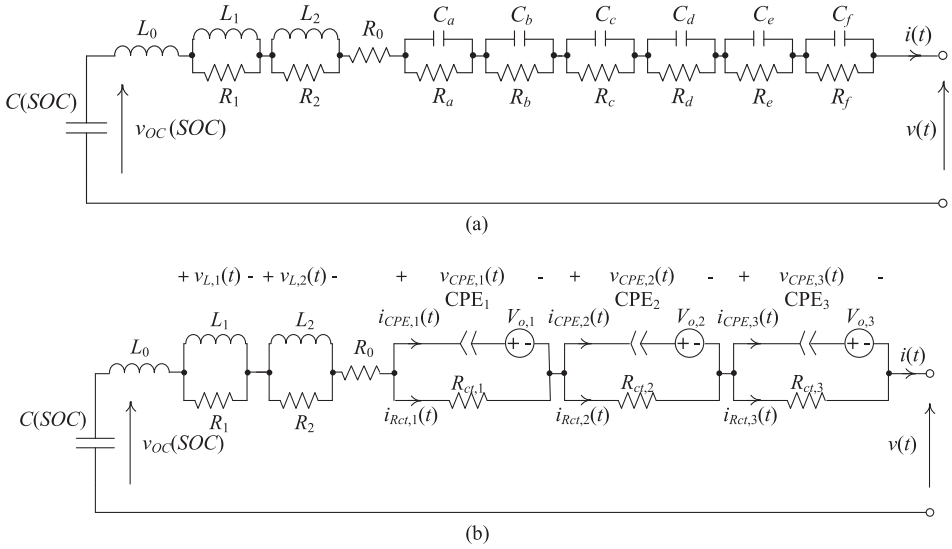

Fig. 1. Battery electrical models with different kinds of impedance networks. (a) With RC networks. (b) With CPEs.

computational model is derived by decomposing the battery current into a series of square or trapezoidal current pulses of a predetermined duration and then superimposing the response of the CPE onto the current pulses. A criterion for ensuring the stability of the mathematical model relative to the duration of each current pulse will be derived. The validity of the model can be determined by comparing the prediction results of a battery model consisting of three CPEs with the measurement results of six different SANYO 18650, 3300-mAh, 3.7-V lithium-ion rechargeable batteries under controlled charging and discharging profiles.

II. Voltage-Current Characteristics of CPE

CPE is commonly used to model the electrical properties of double layer capacitors. Such nonideal capacitive characteristic occur in many types of electrochemical storage devices, such as lithium batteries [11] and supercapacitors [12]–[15]. The response of CPE is modeled by different techniques, such as a parallel RC circuit at a single operating frequency in [16] and time-domain response with constant input excitations in [17]. Instead of representing the CPE with passive components or under a particular operating condition, a computational model that can derive the time-domain response of CPE under arbitrary charging and discharging profiles is proposed.

A. Response to a Single Square Current Pulse

Consider that the CPE is subject to a single square current pulse with the start time $t_x$and end time t_y (see Fig. 2). The magnitude and duration of the pulse are $\hat{I}$and τ, respectively

$$t_y = t_x + \tau. \tag{1}$$

The current pulse i_p can be expressed as

$$i_p(t) = \hat{I}\{u[t - t_x] - u[t - t_y]\} \tag{2}$$

where *u* is the Heaviside step function.

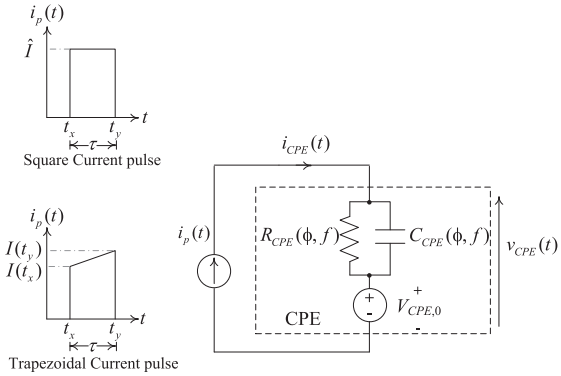

Fig. 2. Single current pulse.

The Laplace-transformed equation of i_p is

$$I_p(s) = \frac{\hat{I}}{s}(e^{-st_x} - e^{-st_y}) \tag{3}$$

where $s = j\omega = j(2\pi f)$ and f is the operating frequency.

Thus, the voltage across the CPE $V_{\mathrm{CPE}}(s)$ is

$$\begin{aligned} V_{\mathrm{CPE}}(s) &= Z_{\mathrm{CPE}}(s)I_p(s) + \frac{V_o}{s} \\ &= \frac{\hat{I}}{s^{\phi+1}C_o}(e^{-st_x} - e^{-st_y}) + \frac{V_o}{s} \end{aligned} \tag{4}$$

where $\phi \in [0, 1]$is defined as the dispersion coefficient C_o is defined as the pseudocapacitance of the double layer $V_o = \begin{cases} V_{\mathrm{CPE},0} & \text{for } \phi > 0 \\ 0 & \text{for } \phi = 0 \end{cases}$ and $V_{\mathrm{CPE},0}$ is the initial voltage on the CPE.

The inverse Laplace-transformed equation of (4) in discrete form is

$$v_{\mathrm{CPE}}[nT] = \frac{\hat{I}}{\Gamma[\phi+1]C_o}\left\{\begin{matrix} u[nT - t_x](nT - t_x)^{\phi} \\ -u[nT - t_y](nT - t_y)^{\phi} \end{matrix}\right\} + V_o, \quad \text{for } nT \geq t_x \tag{5}$$

where Γ is the Gamma function and *T* is the sampling period.

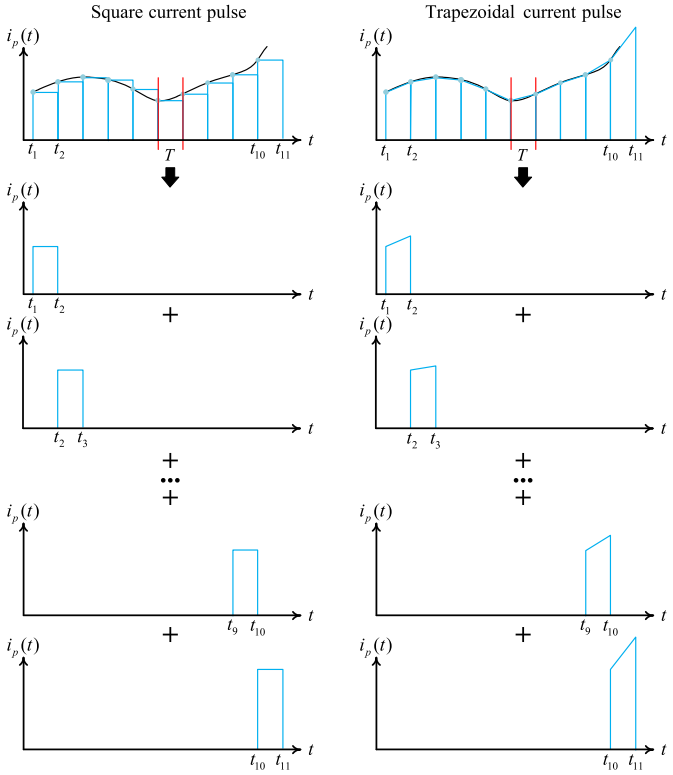

Fig. 3. Decomposition of battery current with the proposed method.

Equation (5) gives the voltage profile of CPE after the CPE is subject to a single square current pulse. The expression is similar to (7) in [17], but with the time delay introduced. Thus, with the CPE current decomposed into a series of square pulses at the sampling time instant kT, as shown in Fig. 3, i_{CPE} can be expressed as

$$i_{\mathrm{CPE}}(t) \approx \sum_{k=0}^{n-1} i_{\mathrm{CPE}}[kT]\{u[t-kT]-u[t-(k+1)T]\}, \quad \text{for } 0 < t \le nT \tag{6}$$

where $i_{\mathrm{CPE}}[kT]$ is the sampled value of i_{CPE} at $t = kT$.

Thus, by using (5), the voltage across the CPE can be expressed as the sum of the voltage profiles caused by a train of current pulses described in (6). That is

$$v_{\mathrm{CPE}}[nT] = \frac{T^{\phi}}{\Gamma[\phi+1]C_o}\sum_{k=0}^{n-1} i_{\mathrm{CPE}}[kT]\begin{Bmatrix}(n-k)^{\phi}\\ -(n-k-1)^{\phi}\end{Bmatrix} + V_o. \tag{7}$$

B. Response to a Single Trapezoidal Current Pulse

As shown in Fig. 3, if the current pulse is modeled by a linear function for $t \in [t_x\ t_y]$

$$i_p(t) = \left\{I(t_x) + \frac{I(t_y)-I(t_x)}{\tau}(t-t_x)\right\}u[t-t_x] - \left\{I(t_y) + \frac{I(t_y)-I(t_x)}{\tau}(t-t_y)\right\}u[t-t_y] \tag{8}$$

where u is the Heaviside step function and $\tau = t_y - t_x$.

The Laplace-transformed equation of i_p is

$$I_p(s) = \left\{\frac{I(t_x)}{s} + \frac{I(t_y)-I(t_x)}{s^2\tau}\right\}e^{-st_x} - \left\{\frac{I(t_y)}{s} + \frac{I(t_y)-I(t_x)}{s^2\tau}\right\}e^{-st_y}. \tag{9}$$

Thus, the voltage across the CPE $V_{\mathrm{CPE}}(s)$ is

$$V_{\mathrm{CPE}}(s) = Z_{\mathrm{CPE}}(s)I_p(s) + \frac{V_o}{s} = \frac{1}{C_o}\left[\begin{array}{l}\dfrac{1}{s^{\phi+1}}\{I(t_x)e^{-st_x} - I(t_y)e^{-st_y}\}\\ +\dfrac{I(t_y)-I(t_x)}{s^{\phi+2}\tau}\{e^{-st_x} - e^{-st_y}\}\end{array}\right] + \frac{V_o}{s} \tag{10}$$

where $V_o = \begin{cases} V_{\mathrm{CPE},0} & \text{for } \phi > 0 \\ 0 & \text{for } \phi = 0 \end{cases}$ and $V_{\mathrm{CPE},0}$ is the initial voltage on the CPE.

The inverse Laplace-transformed equation of (10) in discrete form is

$$v_{\mathrm{CPE}}[nT] = \frac{1}{C_o}\left[\begin{array}{l}\dfrac{1}{\Gamma[\phi+1]}\begin{Bmatrix}I(t_x)(nT-t_x)^{\phi}u[t-t_x]\\ -I(t_y)(nT-t_y)^{\phi}u[nT-t_y]\end{Bmatrix}\\ +\dfrac{I(t_y)-I(t_x)}{\Gamma[\phi+2]\tau}\begin{Bmatrix}(nT-t_x)^{\phi+1}u[nT-t_x]\\ -(nT-t_y)^{\phi+1}u[nT-t_y]\end{Bmatrix}\end{array}\right] + V_o, \quad \text{for } nT \ge t_x. \tag{11}$$

Equation (11) gives the voltage profile of CPE after the CPE is subject to a single trapezoidal current pulse. If the CPE current i_{CPE} is decomposed into a series of trapezoidal pulses at the sampling time instant kT, as shown in Fig. 3, it can be expressed as

$$i_{\mathrm{CPE}}(t) \approx \sum_{k=0}^{n-1}\left[\begin{array}{l}i_{\mathrm{CPE}}[kT]u[t-kT] - i_{\mathrm{CPE}}[k+1T]u[t-(k+1)T]\\ +\dfrac{i_{\mathrm{CPE}}[k+1T]-i_{\mathrm{CPE}}[kT]}{\tau}\begin{Bmatrix}(t-kT)u[t-kT]\\ -(t-(k+1)T)\\ \cdot u[t-(k+1)T]\end{Bmatrix}\end{array}\right], \quad \text{for } 0 < t \le nT \tag{12}$$

where $i_{\mathrm{CPE}}[kT]$ is sampled value of i_{CPE} at $t = kT$.

Thus, by using (11), the voltage across the CPE can be expressed as the sum of the voltage profiles caused by a train of

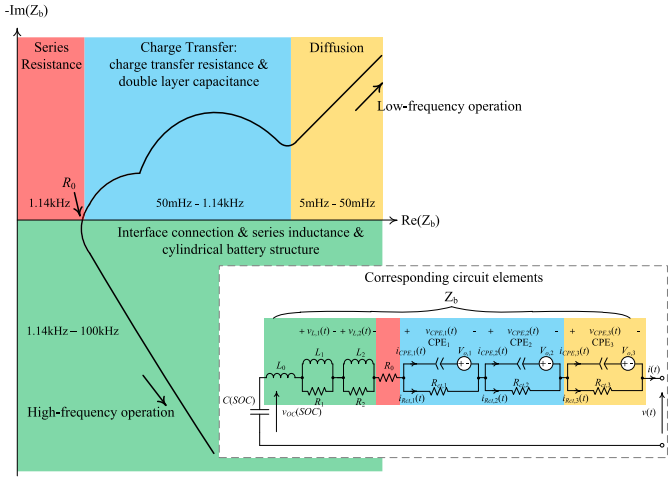

Fig. 4. Nyquist plot of the impedance of typical cylindrical lithium battery.

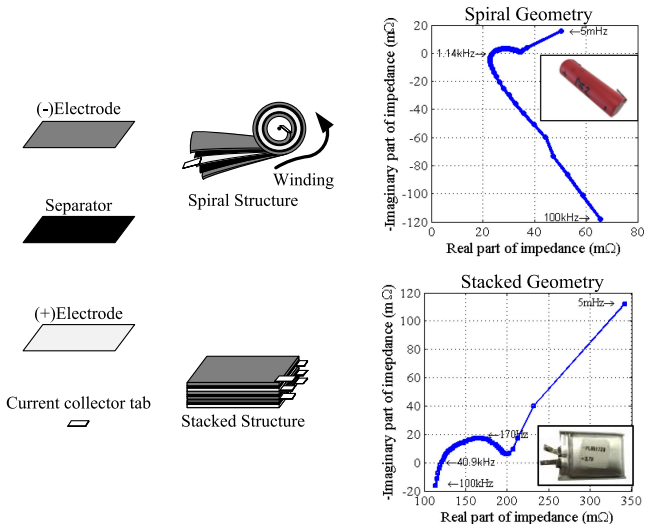

Fig. 5. Physical structures of two batteries and their EIS results. (a) Physical structures. (b) EIS results of the two structures.

current pulses described in (12). That is

$$v_{\mathrm{CPE}}[nT] = \frac{T^{\phi}}{C_o}\sum_{k=0}^{n-1}\left[\begin{array}{l}\dfrac{1}{\Gamma[\phi+1]}\left\{\begin{array}{l} i_{\mathrm{CPE}}[kT](n-k)^{\phi} \\ -i_{\mathrm{CPE}}[k+1T](n-k-1)^{\phi}\end{array}\right\} \\ +\dfrac{i_{\mathrm{CPE}}[k+1T]-i_{\mathrm{CPE}}[kT]}{\Gamma[\phi+2]}\left\{\begin{array}{l}(n-k)^{\phi+1} \\ -(n-k-1)^{\phi+1}\end{array}\right\}\end{array}\right] + V_o. \tag{13}$$

With the battery current decomposed into a train of constant or trapezoidal current pulses, the magnitude of each pulse varies with the value of the actual battery current at each sampling instant. Thus, the waveform of the battery current can be of different shape.

III. Modeling With Multiple CPEs

Fig. 4 shows typical Nyquist plot of the impedance of a cylindrical lithium battery from low to high operating frequency. There are four regions highlighted in different colors. Each one is dominated by a network in the battery model [see Fig. 1(b)]. Two regions exhibiting the behaviors of three CPEs are identified. R_0 characterizes ohmic internal resistance for the electrodes, electrolyte, and separators [18]. $R_{\mathrm{ct},1}$, $R_{\mathrm{ct},2}$, and $R_{\mathrm{ct},3}$ characterize charge transfer resistances in the electrochemical reaction [19]. The three CPEs, including CPE_1, CPE_2, and CPE_3, characterize the double-layer characteristics of charge distribution [16], [20], [21]. Two networks $\mathrm{CPE}_1 - R_{\mathrm{ct},1}$ and $\mathrm{CPE}_2 - R_{\mathrm{ct},2}$ are used to model the charge transfer interaction of the electrodes and electrolyte, which form semicircle trajectories in low frequency [22], [23]. Another network $\mathrm{CPE}_3 - R_{\mathrm{ct},3}$ characterizes ion diffusion phenomenon at very low frequency, forming a "tail" on the impedance plot [23], [24]. L_0 and two parallel *RL* networks characterize the wire, interface connection, and cylindrical battery structure [25]–[27]. Fig. 5(a) shows two common battery designs. They are spiral and stacked structures [25], [26]. The inductance associated with the geometry of the lithium battery contributes significantly to the impedance at high frequency. The inductive characteristics of the stacked geometry design are not as critical as that of the spiral design [see Fig. 5(b)]. This phenomenon can be further explained by considering the current flow and the placement of current collector tabs, as discussed in [28], [29].

By using the Kirchhoff's voltage and current laws, the battery terminal voltage $v(t)$ and terminal current $i(t)$ can be expressed as

$$v(t) = L_0\frac{di(t)}{dt} + v_{L,1}(t) + v_{L,2}(t) + i(t)R_0 + v_{\mathrm{CPE},1}(t) + v_{\mathrm{CPE},2}(t) + v_{\mathrm{CPE},3}(t) \tag{14}$$

$$v_{L,1}(t) = L_1\frac{di(t)}{dt} - \frac{L_1}{R_1}\frac{dv_{L,1}(t)}{dt} \tag{15}$$

$$v_{L,2}(t) = L_2\frac{di(t)}{dt} - \frac{L_2}{R_2}\frac{dv_{L,2}(t)}{dt} \tag{16}$$

$$i(t) = i_{\mathrm{CPE},1}(t) + i_{Rct,1}(t) = i_{\mathrm{CPE},1}(t) + \frac{v_{\mathrm{CPE},1}(t)}{R_{\mathrm{ct},1}} \tag{17}$$

$$i(t) = i_{\mathrm{CPE},2}(t) + i_{R\mathrm{ct},2}(t) = i_{\mathrm{CPE},2}(t) + \frac{v_{\mathrm{CPE},2}(t)}{R_{\mathrm{ct},2}} \tag{18}$$

$$i(t) = i_{\mathrm{CPE},3}(t) + i_{R\mathrm{ct},3}(t) = i_{\mathrm{CPE},3}(t) + \frac{v_{\mathrm{CPE},3}(t)}{R_{\mathrm{ct},3}} \tag{19}$$

where $v_{L,1}$and $v_{L,2}$ are the voltage across L_1 and L_2, respectively, $v_{\mathrm{CPE},1}$, $v_{\mathrm{CPE},2}$, and $v_{\mathrm{CPE},3}$ are the voltages across CPE_1, CPE_2, and CPE_3, respectively, $i_{\mathrm{CPE},1}$, $i_{\mathrm{CPE},2}$, and $i_{\mathrm{CPE},3}$ are the currents through CPE_1, CPE_2,and CPE_3, respectively, and $i_{Rct,1}$, $i_{Rct,2}$, and $i_{Rct,3}$ are the currents through $R_{\mathrm{ct},1}$, $R_{\mathrm{ct},2}$, and $R_{\mathrm{ct},3}$, respectively.

Based on (17)–(19)

$$i_{\mathrm{CPE},1}(t) = i(t) - \frac{v_{\mathrm{CPE},1}(t)}{R_{\mathrm{ct},1}} \tag{20}$$

$$i_{\mathrm{CPE},2}(t) = i(t) - \frac{v_{\mathrm{CPE},2}(t)}{R_{\mathrm{ct},2}} \tag{21}$$

$$i_{\mathrm{CPE},3}(t) = i(t) - \frac{v_{\mathrm{CPE},3}(t)}{R_{\mathrm{ct},3}}. \tag{22}$$

A. Response to a Single Square Current Pulse

Based on (7), (20)–(22), $v_{\mathrm{CPE},1}[nT]$, $v_{\mathrm{CPE},2}[nT]$, and $v_{\mathrm{CPE},3}[nT]$ can be expressed as

$$v_{\mathrm{CPE},1}[nT] = \frac{T^{\phi_1}}{\Gamma[\phi_1+1]C_{o,1}} \times \sum_{k=0}^{n-1}\left\{i[kT] - \frac{v_{\mathrm{CPE},1}[kT]}{R_{\mathrm{ct},1}}\right\}\begin{Bmatrix}(n-k)^{\phi_1}\\ -(n-k-1)^{\phi_1}\end{Bmatrix} + V_{o,1} \tag{23}$$

$$v_{\mathrm{CPE},2}[nT] = \frac{T^{\phi_2}}{\Gamma[\phi_2+1]C_{o,2}} \times \sum_{k=0}^{n-1}\left\{i[kT] - \frac{v_{\mathrm{CPE},2}[kT]}{R_{\mathrm{ct},2}}\right\}\begin{Bmatrix}(n-k)^{\phi_2}\\ -(n-k-1)^{\phi_2}\end{Bmatrix} + V_{o,2} \tag{24}$$

$$v_{\mathrm{CPE},3}[nT] = \frac{T^{\phi_3}}{\Gamma[\phi_3+1]C_{o,3}} \times \sum_{k=0}^{n-1}\left\{i[kT] - \frac{v_{\mathrm{CPE},3}[kT]}{R_{\mathrm{ct},3}}\right\}\begin{Bmatrix}(n-k)^{\phi_3}\\ -(n-k-1)^{\phi_3}\end{Bmatrix} + V_{o,3} \tag{25}$$

where ϕ_1, ϕ_2, and ϕ_3 are the dispersion coefficients of CPE_1, CPE_2, and CPE_3, respectively, $C_{o,1}$, $C_{o,2}$, and $C_{o,3}$ are the double-layer pseudocapacitances of CPE_1, CPE_2, and CPE_3, respectively, and $V_{o,1}$, $V_{o,2}$, and $V_{o,3}$ are the initial voltages across CPE_1, CPE_2, and CPE_3, respectively.

The voltage–current characteristic of the entire impedance network is obtained by putting (23)–(25) into (14).

B. Response to a Single Trapezoidal Current Pulse

By using (13), (20)–(22), $v_{\mathrm{CPE},1}[nT]$, $v_{\mathrm{CPE},2}[nT]$, and $v_{\mathrm{CPE},3}[nT]$can be expressed as

$$v_{\mathrm{CPE},1}[nT] = \frac{T^{\phi_1}}{C_{o,1}}\sum_{k=0}^{n-1}\left\{\frac{1}{\Gamma[\phi_1+1]} \times \begin{bmatrix}(i[kT] - \frac{v_{\mathrm{CPE},1}[kT]}{R_{\mathrm{ct},1}})(n-k)^{\phi_1}\\ -(i[k+1T] - \frac{v_{\mathrm{CPE},1}[kT]}{R_{\mathrm{ct},1}})(n-k-1)^{\phi_1}\end{bmatrix} + \frac{i[k+1T]-i[kT]}{\Gamma[\phi_1+2]}[(n-k)^{\phi_1+1} - (n-k-1)^{\phi_1+1}]\right\} + V_{o,1} \tag{26}$$

$$v_{\mathrm{CPE},2}[nT] = \frac{T^{\phi_2}}{C_{o,2}}\sum_{k=0}^{n-1}\left\{\frac{1}{\Gamma[\phi_2+1]} \times \begin{bmatrix}(i[kT] - \frac{v_{\mathrm{CPE},2}[kT]}{R_{\mathrm{ct},2}})(n-k)^{\phi_2}\\ -(i[k+1T] - \frac{v_{\mathrm{CPE},2}[kT]}{R_{\mathrm{ct},2}})(n-k-1)^{\phi_2}\end{bmatrix} + \frac{i[k+1T]-i[kT]}{\Gamma[\phi_2+2]}[(n-k)^{\phi_2+1} - (n-k-1)^{\phi_2+1}]\right\} + V_{o,2} \tag{27}$$

$$v_{\mathrm{CPE},3}[nT] = \frac{T^{\phi_3}}{C_{o,3}}\sum_{k=0}^{n-1}\left\{\frac{1}{\Gamma[\phi_3+1]} \times \begin{bmatrix}(i[kT] - \frac{v_{\mathrm{CPE},3}[kT]}{R_{\mathrm{ct},3}})(n-k)^{\phi_3}\\ -(i[k+1T] - \frac{v_{\mathrm{CPE},3}[kT]}{R_{\mathrm{ct},3}})(n-k-1)^{\phi_3}\end{bmatrix} + \frac{i[k+1T]-i[kT]}{\Gamma[\phi_3+2]}[(n-k)^{\phi_3+1} - (n-k-1)^{\phi_3+1}]\right\} + V_{o,3}. \tag{28}$$

Similarly, the voltage–current characteristic of the entire impedance network is obtained by putting (26)–(28) into (14).

IV. Stability Analysis

The stability of the derived computational models is analyzed by first deriving second-order characteristic equations and then determining their root locations. The analysis methods for the two types of current pulses are described as follows.

A. With Square Current Pulses

By using (23)–(25), second-order difference equations for $v_{\mathrm{CPE},1}$, $v_{\mathrm{CPE},2}$, and $v_{\mathrm{CPE},3}$ can be expressed as

$$v_{\mathrm{CPE},1}[2T] + \frac{T^{\phi_1}\{v_{\mathrm{CPE},1}[T] + v_{\mathrm{CPE},1}[0](2^{\phi_1}-1)\}}{\Gamma[\phi_1+1]C_{o,1}R_{\mathrm{ct},1}} = \frac{T^{\phi_1}\{i[T] + i[0](2^{\phi_1}-1)\}}{\Gamma[\phi_1+1]C_{o,1}} + V_{o,1} \tag{29}$$

$$v_{\mathrm{CPE},2}[2T] + \frac{T^{\phi_2}\{v_{\mathrm{CPE},2}[T] + v_{\mathrm{CPE},2}[0](2^{\phi_2}-1)\}}{\Gamma[\phi_2+1]C_{o,2}R_{\mathrm{ct},2}} = \frac{T^{\phi_2}\{i[T] + i[0](2^{\phi_2}-1)\}}{\Gamma[\phi_2+1]C_{o,2}} + V_{o,2} \tag{30}$$

$$v_{\mathrm{CPE},3}[2T] + \frac{T^{\phi_3}\{v_{\mathrm{CPE},3}[T] + v_{\mathrm{CPE},3}[0](2^{\phi_3}-1)\}}{\Gamma[\phi_3+1]C_{o,3}R_{\mathrm{ct},3}} = \frac{T^{\phi_3}\{i[T] + i[0](2^{\phi_3}-1)\}}{\Gamma[\phi_3+1]C_{o,3}} + V_{o,3}. \tag{31}$$

The characteristic equations of (29)–(31) in z-domain are expressed as

$$z^2 + \frac{T^{\phi_1}}{\Gamma[\phi_1+1]C_{o,1}R_{\mathrm{ct},1}}z + \frac{T^{\phi_1}}{\Gamma[\phi_1+1]C_{o,1}R_{\mathrm{ct},1}}(2^{\phi_1}-1) = 0 \tag{32}$$

$$z^2 + \frac{T^{\phi_2}}{\Gamma[\phi_2+1]C_{o,2}R_{\mathrm{ct},2}}z + \frac{T^{\phi_2}}{\Gamma[\phi_2+1]C_{o,2}R_{\mathrm{ct},2}}(2^{\phi_2}-1) = 0 \tag{33}$$

$$z^2 + \frac{T^{\phi_3}}{\Gamma[\phi_3+1]C_{o,3}R_{\mathrm{ct},3}}z + \frac{T^{\phi_3}}{\Gamma[\phi_3+1]C_{o,3}R_{\mathrm{ct},3}}(2^{\phi_3}-1) = 0. \tag{34}$$

Thus, the roots of (32)–(34) are

$$z_{\mathrm{CPE}1} = \frac{-K_1 \pm \sqrt{{K_1}^2 - 4K_1(2^{\phi_1}-1)}}{2} \tag{35}$$

$$z_{\mathrm{CPE}2} = \frac{-K_2 \pm \sqrt{{K_2}^2 - 4K_2(2^{\phi_2}-1)}}{2} \tag{36}$$

$$z_{\mathrm{CPE}3} = \frac{-K_3 \pm \sqrt{{K_3}^2 - 4K_3(2^{\phi_3}-1)}}{2} \tag{37}$$

where $K_1 = \frac{T^{\phi_1}}{\Gamma[\phi_1+1]C_{o,1}R_{\mathrm{ct},1}}$, $K_2 = \frac{T^{\phi_2}}{\Gamma[\phi_2+1]C_{o,2}R_{\mathrm{ct},2}}$, and $K_3 = \frac{T^{\phi_3}}{\Gamma[\phi_3+1]C_{o,3}R_{\mathrm{ct},3}}$.

According to the stability criterion for discrete-time system [30], the derived time-domain model is stable if and only if the roots in (35)–(37) are all within the unit circle.

B. With Trapezoidal Current Pulses

By using (26)–(28), the second-order difference equations for $v_{\mathrm{CPE},1}$, $v_{\mathrm{CPE},2}$, and $v_{\mathrm{CPE},3}$ are expressed as

$$v_{\mathrm{CPE},1}[2T] + \frac{T^{\phi_1}}{\Gamma[\phi_1+1]C_{o,1}R_{\mathrm{ct},1}}\left\{\begin{matrix} v_{\mathrm{CPE},1}[T] \\ +v_{\mathrm{CPE},1}[0](2^{\phi_1}-1)\end{matrix}\right\}$$
$$= \frac{T^{\phi_1}}{\Gamma[\phi_1+2]C_{o,1}}\{i[2T]+i[T](2^{\phi_1+1}-2)-i[0](2^{\phi_1+1}-1)\} + \frac{T^{\phi_1}}{\Gamma[\phi_1+1]C_{o,1}}i[0](2^{\phi_1}) + V_{o,1} \tag{38}$$

$$v_{\mathrm{CPE},2}[2T] + \frac{T^{\phi_2}}{\Gamma[\phi_2+1]C_{o,2}R_{\mathrm{ct},2}}\left\{\begin{matrix} v_{\mathrm{CPE},2}[T] \\ +v_{\mathrm{CPE},2}[0](2^{\phi_2}-1)\end{matrix}\right\}$$
$$= \frac{T^{\phi_2}}{\Gamma[\phi_2+2]C_{o,2}}\{i[2T]+i[T](2^{\phi_2+1}-2)-i[0](2^{\phi_2+1}-1)\} + \frac{T^{\phi_2}}{\Gamma[\phi_2+1]C_{o,2}}i[0](2^{\phi_2}) + V_{o,2} \tag{39}$$

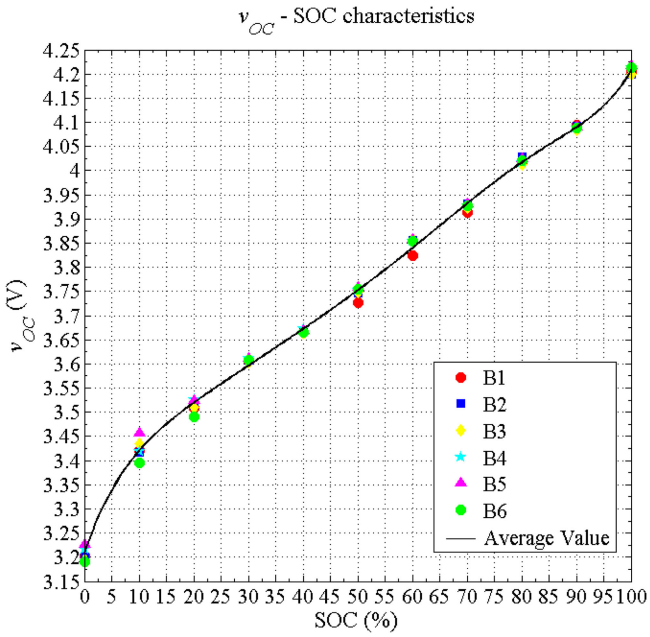

Fig. 6. v_{oc}—SOC characteristics of B1–B6.

$$v_{\mathrm{CPE},3}[2T] + \frac{T^{\phi_3}}{\Gamma[\phi_3+1]C_{o,3}R_{\mathrm{ct},3}}\left\{\begin{matrix} v_{\mathrm{CPE},3}[T] \\ +v_{\mathrm{CPE},3}[0](2^{\phi_3}-1)\end{matrix}\right\}$$
$$= \frac{T^{\phi_3}}{\Gamma[\phi_3+2]C_{o,3}}\{i[2T]+i[T](2^{\phi_3+1}-2)-i[0](2^{\phi_3+1}-1)\} + \frac{T^{\phi_3}}{\Gamma[\phi_3+1]C_{o,3}}i[0](2^{\phi_3}) + V_{o,3}. \tag{40}$$

The characteristic equations of (38)–(40) in z-domain are found to be the same as (32)–(34), respectively. Thus, the stability criteria are the same as that of the model derived with square current pulses.

V. Experimental Verifications

The derived computational models are evaluated by comparing the predicted time-domain waveforms of six lithium batteries under arbitrary charging and discharging profiles with the actual waveforms. In addition, their accuracies are compared with that of the battery models using two, four, and six parallel RC networks. The six batteries, labeled as B1–B6, are all SANYO 18650, 3300-mAh, 3.7-V, rechargeable Li-ion batteries. Each one is tested by placing it in a test fixture with four-wire connections [31].

The frequency characteristics of the batteries are tested by conducting EIS on the electrochemical workstation ZAHNER IM6 [32], [33]. The batteries are tested by injecting sinusoidal perturbations with peak-to-peak amplitude of 5 mV and frequency varying from 5 mHz to 100 kHz with the bias voltage equal to the open circuit voltage v_{OC}. The frequency characteristics of the batteries with the SOC varying from 0% to 100% are studied in step of 10%. Fig. 6 shows the measured $v_{\mathrm{OC}}-$SOC characteristics, obtained by the voltage relaxation method, described in [34]–[36]. Figs. 7 and 8 show the Nyquist plots of

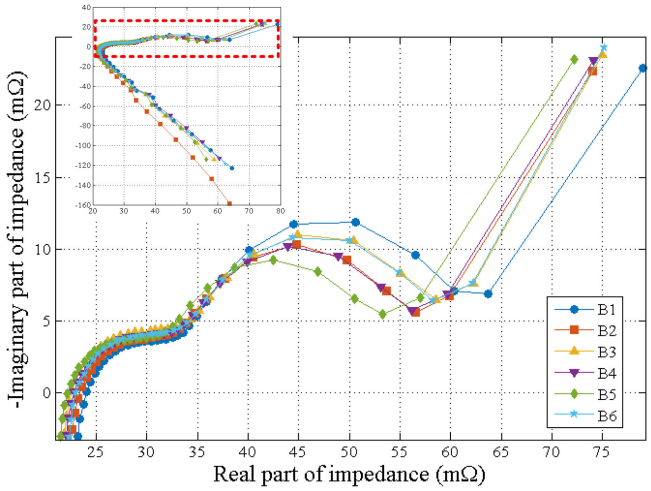

Fig. 7. Nyquist plots of the impedances of the six batteries for SOC = 100%.

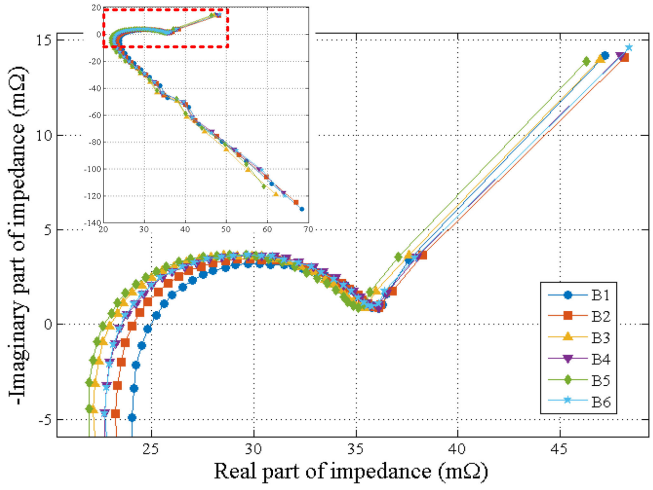

Fig. 8. Nyquist plots of the impedances of the six batteries for SOC = 30%.

the measured battery impedances for SOC=100% and 30%, respectively.

Fig. 9 shows the EIS measurements of different batteries under different SOCs. The intrinsic parameters vary with SOC, particularly R_0 and low-frequency impedance; R_0 reduces as SOC increases. The span of the semicircles is widened at the low and high values of SOC [37]. Thus, high-order battery models are needed to characterize battery behaviors.

Fig. 10 shows four battery models used for fitting EIS measurements. Fig. 11 shows the results fitted with different impedance networks, including two, four, or six parallel RC, or three CPE–$R_{\rm ct}$ networks. Fig. 12 shows the magnified regions marked in Fig. 11. The curve fitting method is based on the complex nonlinear least square algorithm [38] by the Scribner Associates ZView software. The SOC changes from 0% to 100% in steps of 20%. The average chi-square goodness of fit of three CPEs, six RCs, four RCs, and two RCs are 3.25e−5, 3.68e−5, 1.37e−4, and 2.63e−3, respectively. The results reveal that the accuracy of the models with parallel RC networks increases, as the network order increases. However, the model with six parallel RC networks can well fit high-frequency characteristics, but not low-frequency characteristics, implying that the model cannot predict low-frequency behavior accurately. The model with three CPEs can fit both low and high frequency characteristics accurately.

Fig. 13 shows the estimated parameters of the model with three CPEs. As SOC increases, $R_o$and ϕ_3 reduce. The widened span of the semicircles under low SOC and high SOC is reflected by the variations of the pseudocapacitance $C_{o,2}$, dispersion factor ϕ_2, and charge transfer resistance $R_{{\rm ct},2}$, which show U-shaped and W-shaped changes. Fig. 14 shows the trajectories of CPE_2–$R_{{\rm ct},2}$ based on these three parameters with SOC = 0%, 50%, and 100%, respectively. When SOC = 50%, CPE_2–$R_{{\rm ct},2}$ forms a quarter circle trajectory with excitation frequency varying from 80 to 0.1 Hz. The values of $C_{o,2}$, ϕ_2, and $R_{{\rm ct},2}$ are $1.291\mathrm{Fs}^{(\phi_2-1)}$, 0.655, and 0.143 mΩ, respectively. When SOC = 0% or 100%, CPE_2–$R_{{\rm ct},2}$ form a semicircle trajectory with larger values of $C_{o,2}$, ϕ_2, and $R_{{\rm ct},2}$. They are $12.1\mathrm{Fs}^{(\phi_2-1)}$, 0.893, and 0.168 mΩ, respectively, for SOC = 0% and $7.04\mathrm{Fs}^{(\phi_2-1)}$, 0.906, and 0.187 mΩ, respectively, for SOC = 100%. It can be seen that the trajectory is expanded as a semicircle when the values of $C_{o,2}$, ϕ_2, and $R_{{\rm ct},2}$ are large, while the trajectory becomes a quarter circle when the values are small. L_0 and the parameters of the *RL* parallel networks are nearly constant.

Based on the estimated parameters, the time-domain waveforms with different models under arbitrary current profile are calculated. The test setup for performing charging and discharging processes with different current profiles is given in [39]. Fig. 15 shows a testing current profile, including both charging and discharging processes. The current profile contains high and low frequency pulses. Fig. 16 shows the simulated voltage waveforms with the four models for the battery B3. Fig. 17 shows the magnified regions marked in Fig. 16. Fig. 18 shows the percentage error between the simulation and measurement results. Fig. 19 shows the cumulative RMS errors. The discrepancies obtained by RC networks are higher than that with the proposed model.

Fig. 20 shows the distribution of the poles of the three CPE–$R_{\rm ct}$ units, obtained by (35)–(37), with different values of *T*. For the $\mathrm{CPE}_1 - R_{{\rm ct},1}$ unit, the roots are outside the unit circle when $T > 1$ ms for SOC 20% and $T > 0.1$ ms for SOC 70%. For the $\mathrm{CPE}_2 - R_{{\rm ct},2}$ and $\mathrm{CPE}_3 - R_{{\rm ct},3}$ units, all roots are within the unit circle even if $T = 1$ ms. Thus, the stability of the proposed computational model is determined by the $\mathrm{CPE}_1 - R_{{\rm ct},1}$ unit.

Fig. 21 shows the estimated responses of the three CPEs with different *T*. The response of $\mathrm{CPE}_1 - R_{{\rm ct},1}$ diverges, when $T > 1$ ms at SOC = 20%, and $T > 0.1$ ms at SOC 70%, confirming the prediction in Fig. 20. Besides, the estimated responses of CPE_2 and CPE_3 with $T = 0.1$, 1, and 3 ms are similar, confirming the validity of stability analysis.

Fig. 22 shows the RMS errors with the square pulses and trapezoidal pulses in the modeling. Results show that the proposed model with trapezoidal pulses can retain high accu-

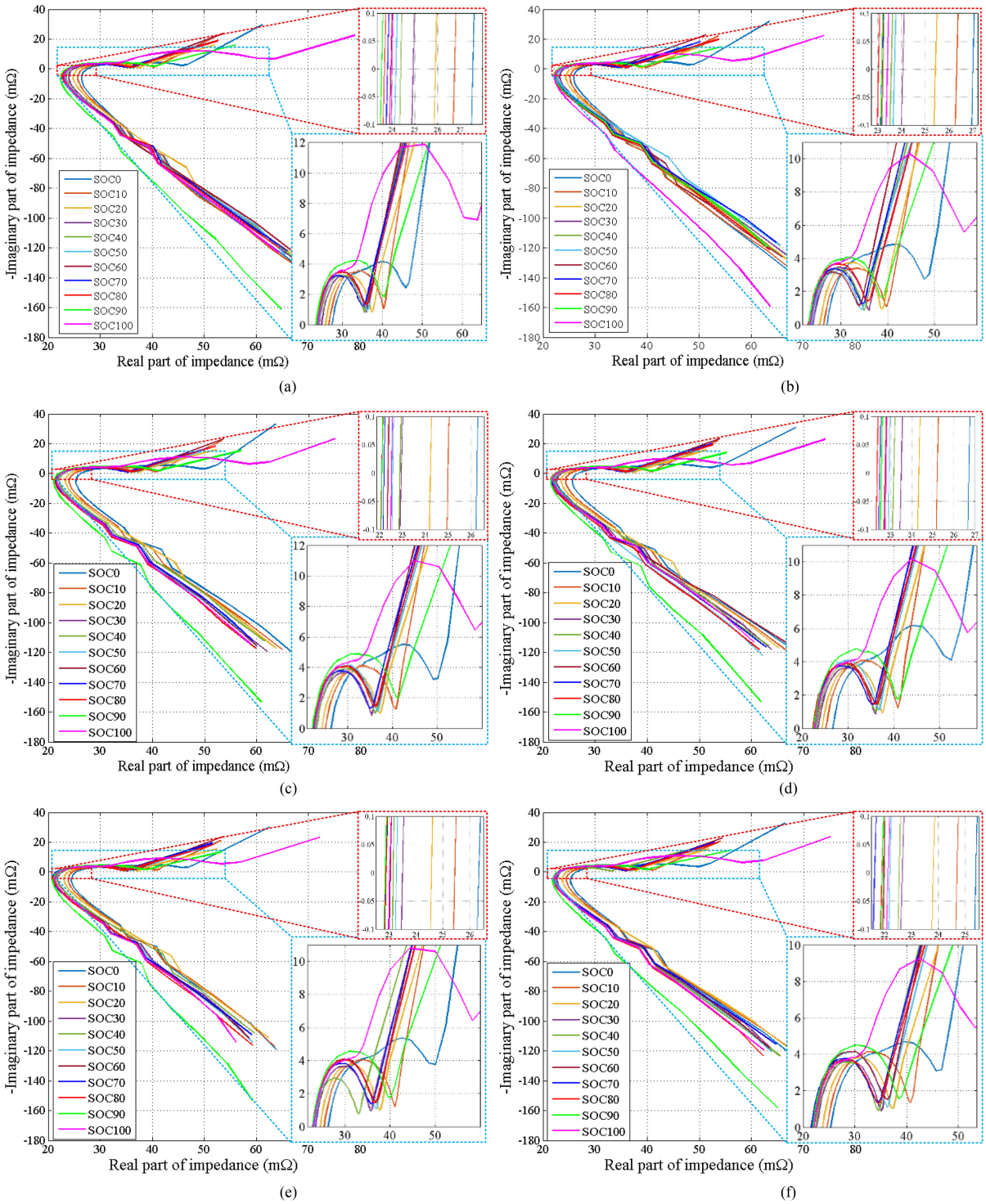

Fig. 9. EIS Nyquist plot of batteries under test with different SOCs. (a) B1. (b) B2. (c) B3. (d) B4. (e) B5. (f) B6.

racy even if the sampling period T increases. Moreover, the computational speed can be shortened with trapezoidal current pulses as the pulse duration can be made longer with trapezoidal current pulses for the same RMS error.

The computation time of proposed models is studied with graphical cards Nvidia Tesla K80, in order to compare the computational complexity between RC networks and CPEs. Fig. 23 shows the computation time and the corresponding RMS errors with different T. Results show that RMS errors with six RC networks are nearly constant and the computation time reduces when T increases.

The computation time with the proposed computational model reduces from 808 to 8.86 s, when T decreases from 0.1 to 1.2 ms. With T=1.2 ms, the RMS errors and the com-

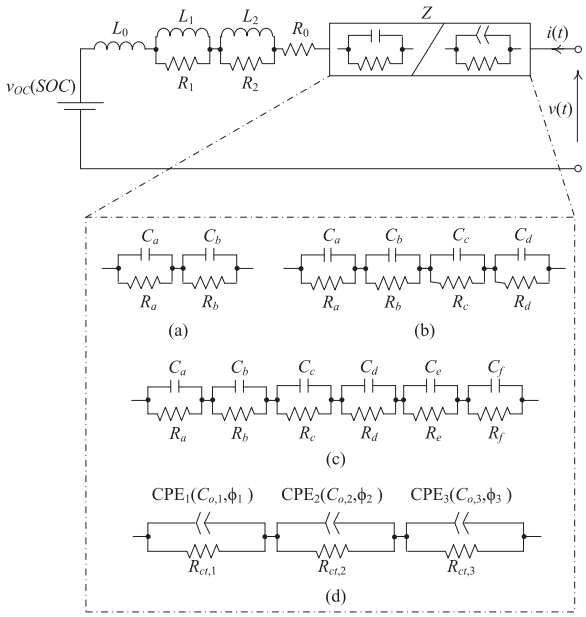

Fig. 10. Battery equivalent circuit models. (a) Two RCs. (b) Four RCs. (c) Six RCs. (d) Three CPEs.

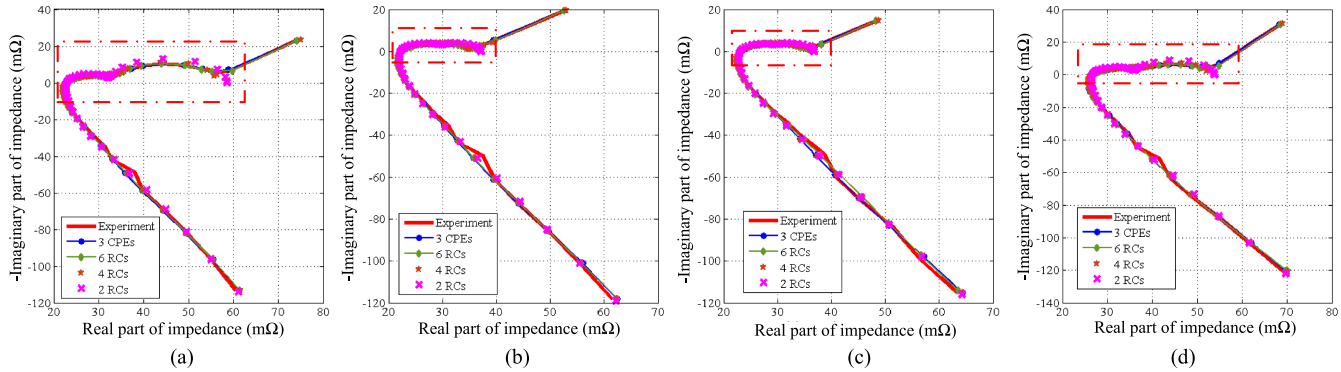

Fig. 11. Curve fitting of EIS measurement results with different impedance models. (a) SOC = 100%. (b) SOC = 80%. (c) SOC = 40%. (d) SOC = 0%.

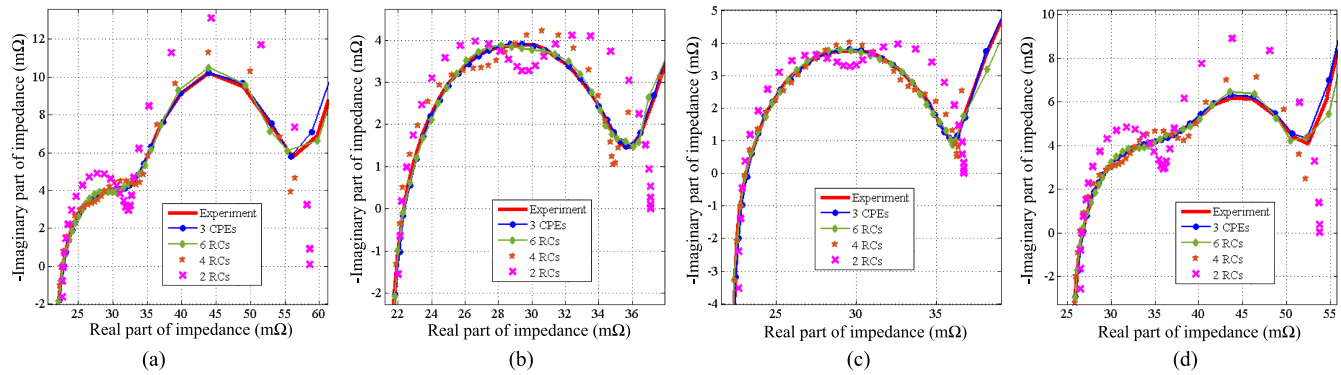

Fig. 12. Magnified regions marked in Fig. 11. (a) SOC = 100%. (b) SOC = 80%. (c) SOC = 40%. (d) SOC = 0%.

putation time with six RC networks are 0.0657% and 6.05 s, respectively. With T=1.6 ms, the RMS errors and the computation time of CPEs are 0.0544% and 5.66 s, respectively. It can be concluded that the proposed model can give a higher accuracy than six RC networks with similar computation time.

VI. Discussions

The effects of the inductive elements and the number of CPE units used in modeling the Li-ion batteries are discussed in the following.

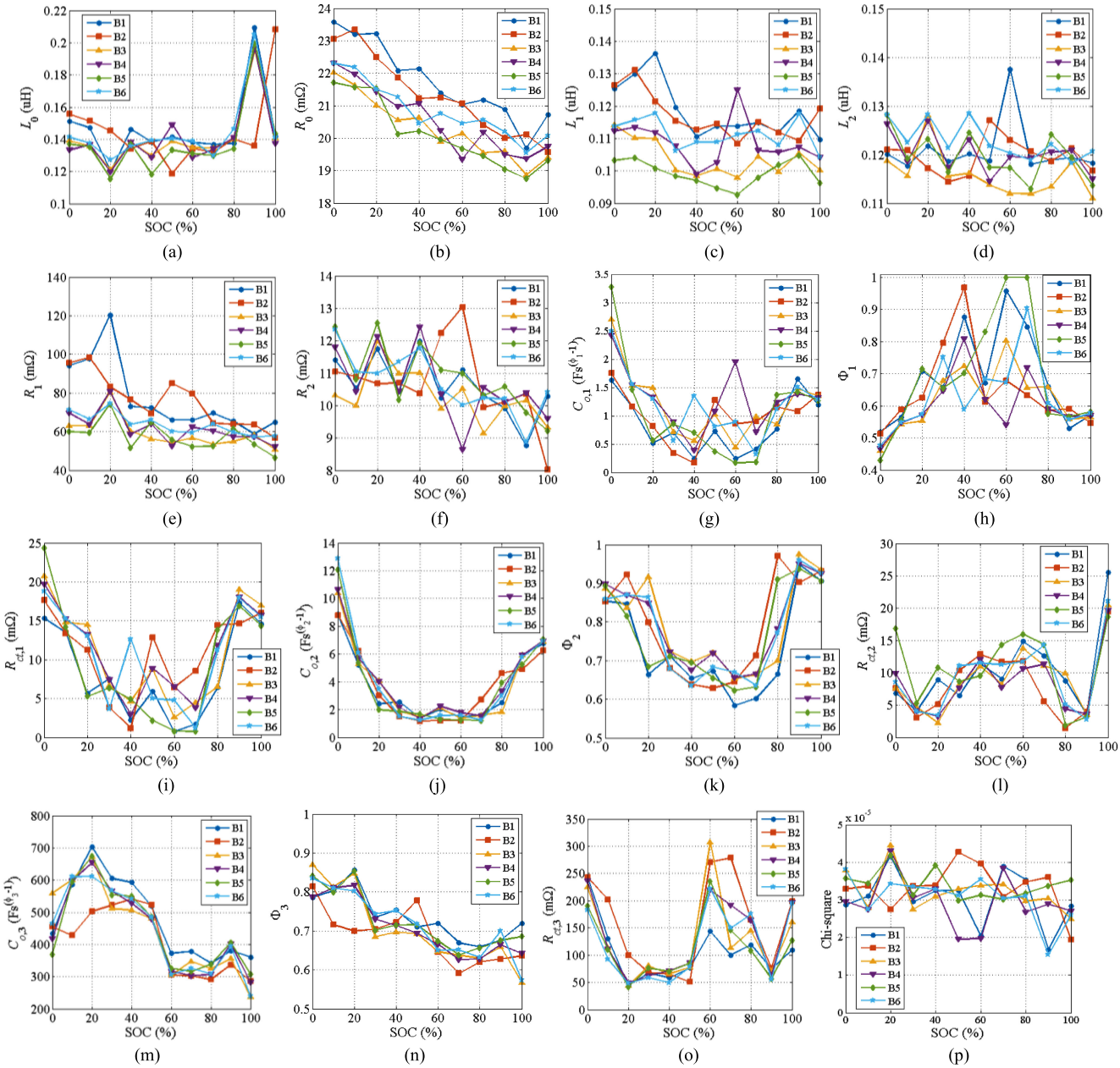

Fig. 13. Estimated parameters with three CPEs under different SOCs. (a) L_0. (b) R_0. (c) L_1. (d) L_2. (e) R_1. (f) R_2. (g) $C_{o,1}$. (h) ϕ_1. (i) $R_{\mathrm{ct},1}$. (j) $C_{o,2}$. (k) ϕ_2. (l) $R_{\mathrm{ct},2}$. (m) $C_{o,3}$. (n) ϕ_3. (o) $R_{\mathrm{ct},3}$. (p) Chi-square.

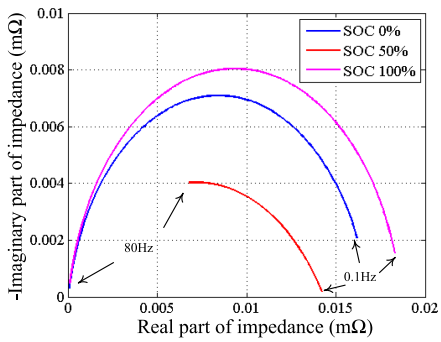

Fig. 14. Variation of $\mathrm{CPE}_2 - R_{\mathrm{ct},2}$ under different SOCs.

A. *Effects of the Inductive Elements*

Prior-art battery modeling techniques ignore inductive characteristics, as the battery under test is typically operated at dc or low frequency [21]–[23], [40]. However, many modern power electronics applications, such as electric vehicles [41], [42], uninterrupted power supplies [43], contactless chargers [44], and photovoltaic systems [45], are operated at high frequency. Thus, models without taking inductive elements into account are unable to estimate battery response accurately. Fig. 24 shows the measured impedance characteristics, predicted impedance characteristics with three CPEs in series with and without the series inductance L_0, and our proposed model. The inductive

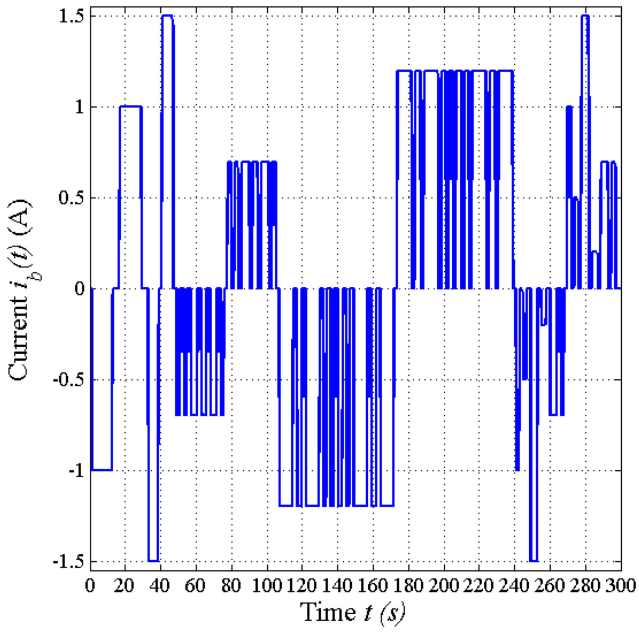

Fig. 15. Current profile.

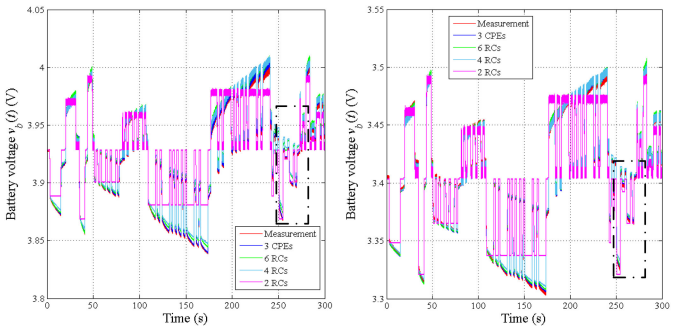

Fig. 16. Time-domain simulation results with different models. (a) SOC = 70%. (b) SOC = 10%.

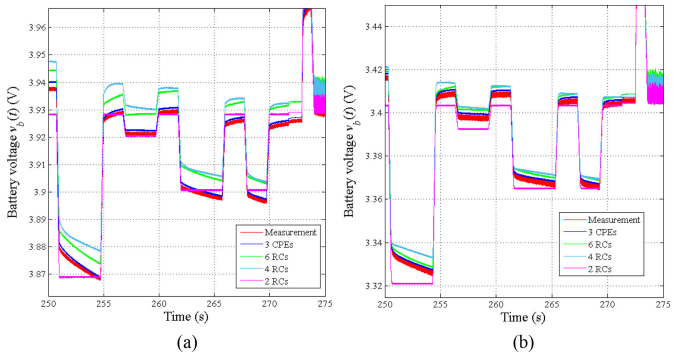

Fig. 17. Magnified results in Fig. 16. (a) SOC = 70%. (b) SOC = 10%.

characteristics become dominant, when the operating frequency is above 2.24 kHz, which is not high in modern power electronics applications. In other words, it is thus crucial to consider inductive characteristics. Results show that all models are

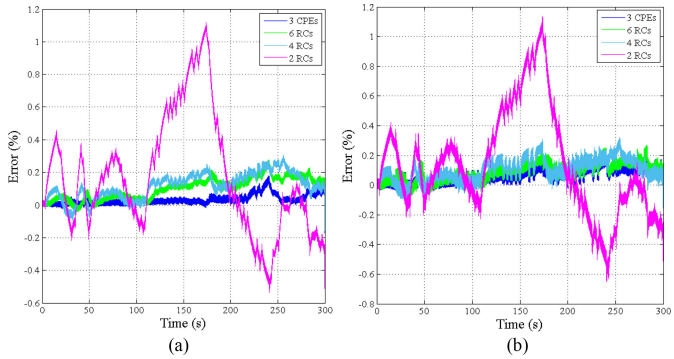

Fig. 18. Time-domain simulation errors. (a) SOC=70%. (b) SOC=10%.

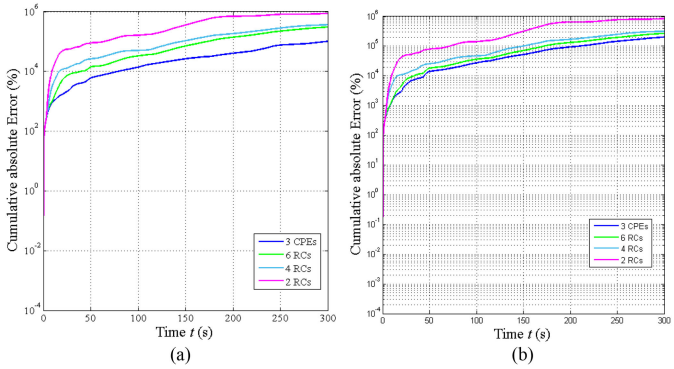

Fig. 19. Cumulative errors. (a) SOC=70%. (b) SOC=10%.

accurate when the operating frequency is between 5 mHz and 915 Hz. However, when the operating frequency is higher than 915 Hz, the proposed model becomes more accurate than the others. Further research will focus on using fractional inductance to represent inductance characteristics [46] to improve accuracy.

B. Effects of the Number of CPE Units

As shown in Fig. 4, two CPEs, CPE1 and CPE2, are used to model impedance characteristics (i.e., the blue region), due to the charge transfer resistance and double layer capacitance, and one CPE, CPE3, is used to model impedance characteristics (i.e., yellow region), due to diffusion. As mentioned in [18] and [47], the frequency characteristics of CPE–$R_{\rm ct}$ networks reflect porous nature of electrode materials and ion concentration in electrolyte under different excitations. Battery models with one CPE, two CPEs, three CPEs, and four CPEs for modeling an 18650 Li-ion battery are compared with the measurement results obtained by EIS. The results are shown in Figs. 25 and 26. The goodness of fit of the models with one CPE, two CPEs, three CPEs, and four CPEs are 2.09e−3, 7.98e−4, 1.96e−5, and 1.94e−5, respectively. The accuracy increases as the number of CPE increases. However, the accuracies with three CPEs and four CPEs are similar. Thus, the battery model with three CPEs gives a good balance among detail, accuracy, and circuit complexity.

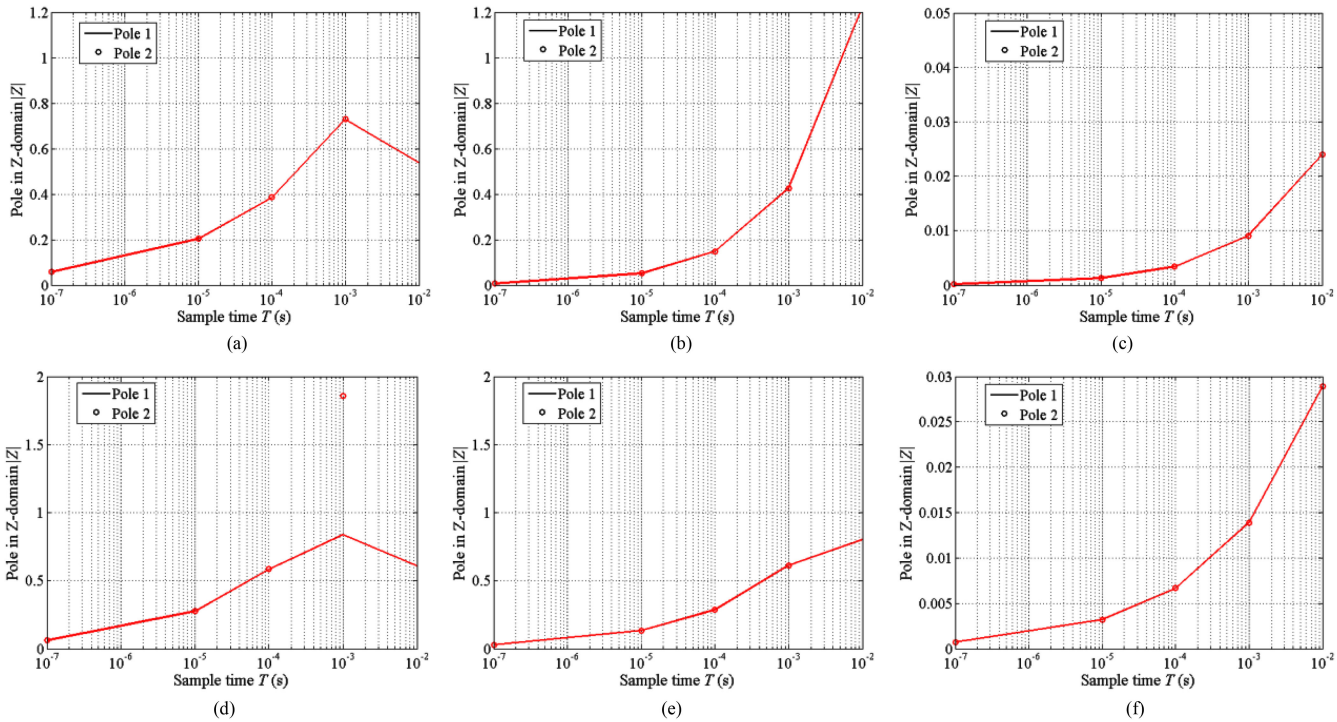

Fig. 20. Pole locations of the three CPE$-R_{ct}$ units under different T. (a) CPE1$-\mathrm{R}_{\mathrm{ct},1}$ at SOC $=$ 20%. (b) $\mathrm{CPE}_2-\mathrm{R}_{\mathrm{ct},2}$ at SOC $=$ 20%. (c) $\mathrm{CPE}_3-\mathrm{R}_{\mathrm{ct},3}$ at SOC $=$ 20%. (d) $\mathrm{CPE}_1-\mathrm{R}_{\mathrm{ct},1}$ at SOC $=$ 70%. (e) $\mathrm{CPE}_2-\mathrm{R}_{\mathrm{ct},2}$ at SOC $=$ 70%. (f) $\mathrm{CPE}_3-\mathrm{R}_{\mathrm{ct},3}$ at SOC $=$ 70%.

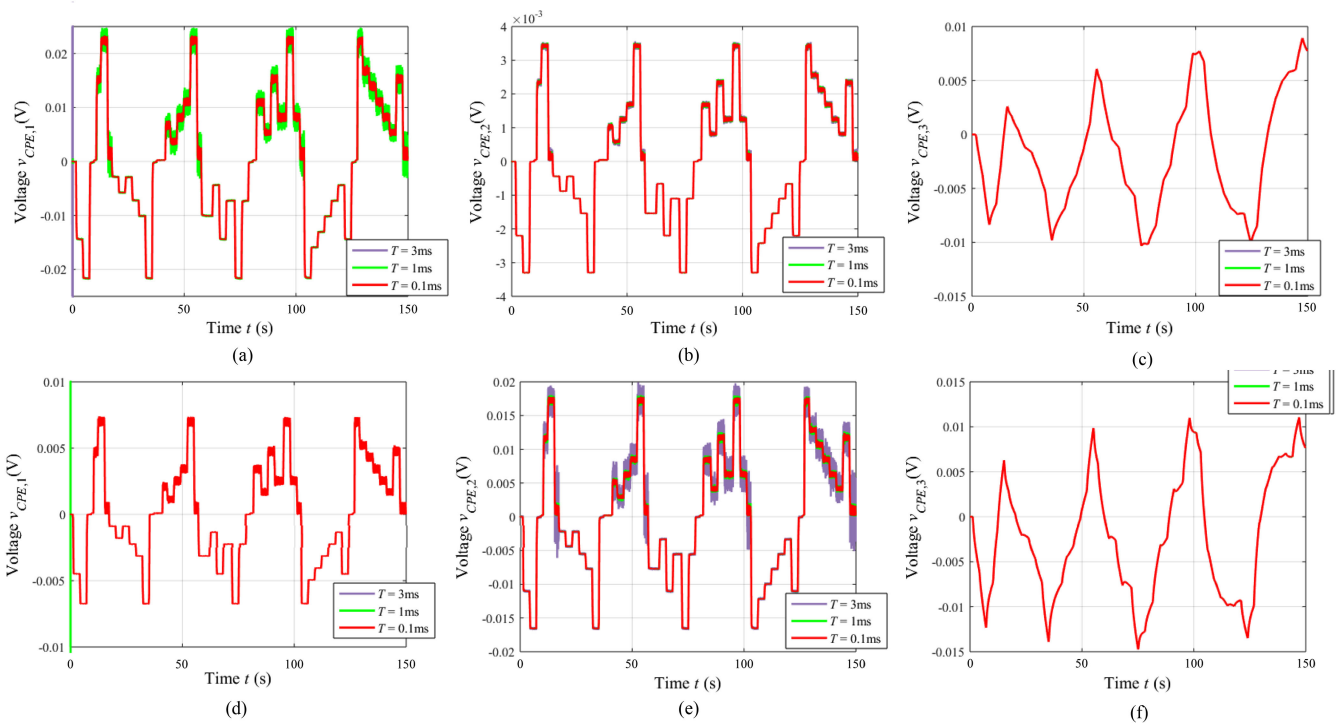

Fig. 21. Voltage responses of three CPEs with different T. (a) CPE_1 at SOC $=$ 20%. (b) CPE_2 at SOC $=$ 20%. (c) CPE_3 at SOC $=$ 20%. (d) CPE_1 at SOC $=$ 70%. (e) CPE_2 at SOC $=$ 70%. (f) CPE_3 at SOC $=$ 70%.

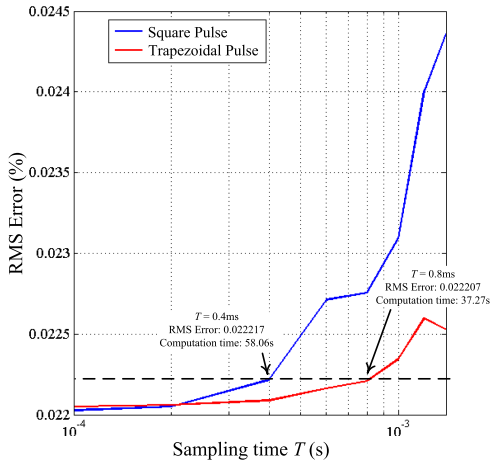

Fig. 22. RMS errors with different modeling techniques.

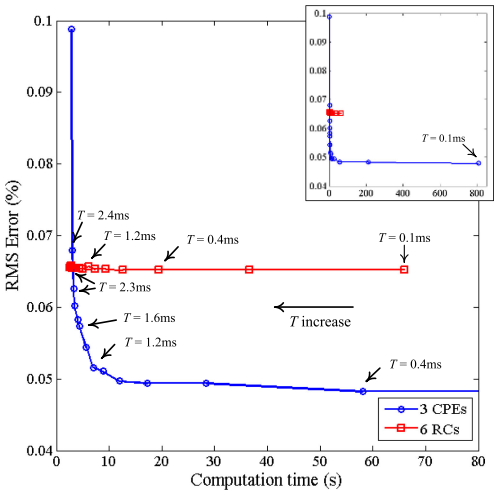

Fig. 23. RMS errors and computational time with different models.

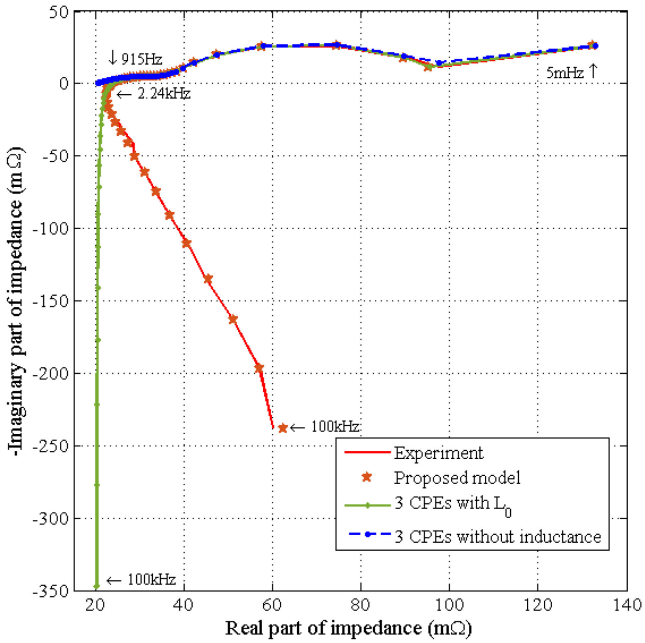

Fig. 24. Impedance simulation results with different models.

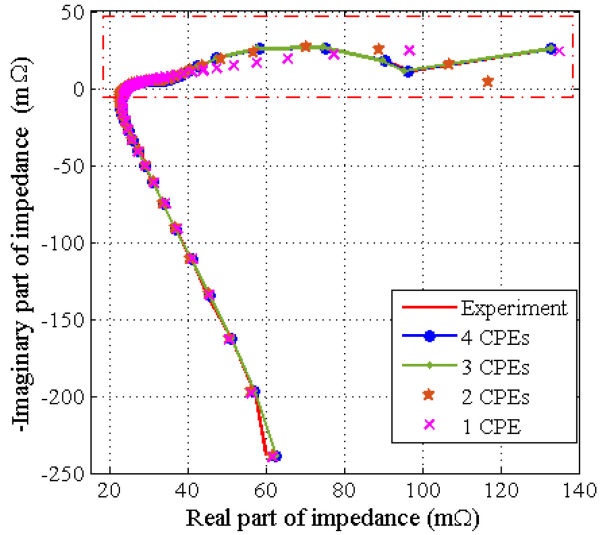

Fig. 25. Curve fitting of EIS measurement results with different CPE units.

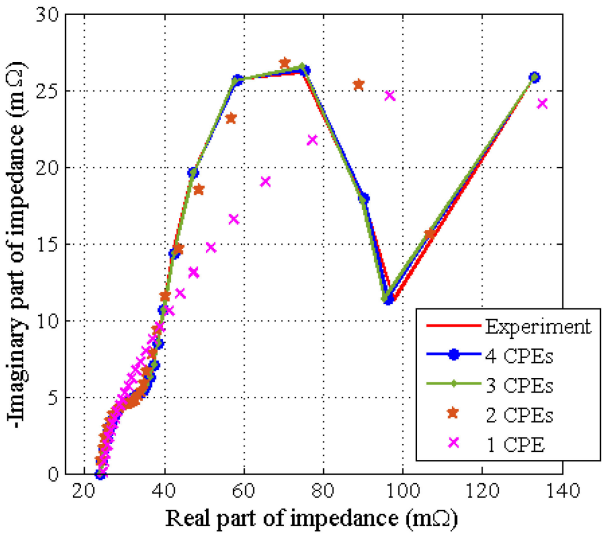

Fig. 26. Magnified regions marked in Fig. 25.

VII. Conclusion

A time-domain model for characterizing the voltage–current characteristics of lithium batteries under arbitrary charging and discharging profiles has been presented. By formulating the time-domain response of a CPE under arbitrary current excitation, multiple CPEs with charge transfer resistance have been applied for constituting a battery model. Detailed derivation of the computational model has been given. The proposed model has been validated by comparing the prediction results of a battery model with the measurement results under controlled charging and discharging profiles. In order to investigate the importance of using CPE units to characterize lithium battery performance, different orders of RC network have been analyzed as well. Results show that the prediction results of three CPE units are more accurate than the RC networks. The criteria for ensuring stability of the computational model have also been derived and confirmed with experiment results. In addition, experiments have revealed that the computation time of proposed

model can effectively reduce and retain high accuracy by using high sampling period.

The proposed model can be further used to predict battery response with the sensed battery current in practical applications. Together with some intrinsic parameter estimation techniques, such as the one in [3], it is possible to estimate the intrinsic parameters of the battery for studying aging issue and parametric sensitivity analysis. Therefore, the proposed time-domain mathematical model lays the foundation for other scientific research on the properties of lithium-ion batteries.

REFERENCES

[1] C. Sinkaram, K. Rajakumar, and V. Asirvadam, "Modeling battery management system using the lithium-ion battery," in *Proc. IEEE Int. Conf. Control Syst., Comput. Eng.*, 2012, pp. 50–55.

[2] E. Chiodo, L. P. Di Noia, and D. Lauria, "Stochastic modelling of electrochemical batteries for smart grids applications," in *Proc. Int. Symp. Power Electron., Elect. Drives, Automat. Motion*, 2014, pp. 1071–1076.

[3] W. Wang, H. Chung, and J. Zhang, "Near-real-time parameter estimation of an electrical battery model with multiple time constants and SOC-dependent capacitance," *IEEE Trans. Power Electron.*, vol. 29, no. 11, pp. 5905–5920, Nov. 2014.

[4] B. Sang, J. Hu, G. Li, J. Xue, and J. Ye, "Equivalent modeling method of battery energy storage system in multi-time scales," in *Proc. IEEE 8th Int. Power Electron. Motion Control Conf.*, 2016, pp. 252–256.

[5] S. Buller, M. Thele, R. W. A. A. De Doncker, and E. Karden, "Impedance-based simulation models of supercapacitors and Li-Ion batteries for power electronic applications," *IEEE Trans. Ind. Appl.*, vol. 41, no. 3, pp. 742–747, May/Jun. 2005.

[6] J. Valsa and J. Vlach, "RC models of a constant phase element," *Int. J. Circuit Theory Appl.*, vol. 41, no. 1, pp. 59–67, Jan. 2013.

[7] B. Hirschorn, M. E. Orazem, B. Tribollet, V. Vivier, I. Frateure, and M. Musiani, "Constant-phase-element behavior caused by resistivity distributions in films," *J. Electrochemical Soc.*, vol. 157, no. 12, pp. 458–463, Oct. 2010.

[8] U. Troltzsch, P. Buschel, and O. Kanoun, "Time domain simulations of constant phase elements using IIR filter," in *Lecture Notes Impedance Spectroscopy: Measurement, Modeling and Applications*. AK Leiden, The Netherlands: CRC Press, ch. 2, 2011.

[9] J. L. Garcia and R. P. Areny, "Measurement of three independent components in impedance sensors using a single square," *Sensors Actuators A*, vol. 110, no. 1–3, pp. 164–170, Feb. 2004.

[10] J. L. Garcia and R. P. Areny, "Constant-phase element identification in conductivity sensors using a single square wave," *Sensors Actuators A*, vol. 132, pp. 122–128, May 2006.

[11] Y. Ma, X. Zhou, B. Li, and H. Chen, "Fractional modeling and soc estimation of lithium-ion battery," *J. Automatica Sinica*, vol. 3, no. 3, pp. 281–288, Jul. 2016.

[12] A. Lasia, *Electrochemical Impedance Spectroscopy and its Applications*. New York, NY, USA: Springer-Verlag, 2014.

[13] A. Allagui, A. S. Elwakil, B. J. Maundy, and T. J. Freeborn, "Spectral capacitance of series and parallel combinations of supercapacitors," *Chem. Electro. Chem.*, vol. 3, no. 9, pp. 1429–1436, Sep. 2016.

[14] A. Allagui, A. S. Elwakil, and T. J. Freeborn, "Supercapacitor reciprocity and response to linear current and voltage ramps," *Electrochim. Acta.*, vol. 258, pp. 1081–1085, Dec. 2017.

[15] A. Allagui, A. S. Elwakil, M. E. Fouda, and A. G. Radwan, "Capacitive behavior and stored energy in supercapacitors at power line frequencies," *J. Power Sources*, vol. 390, pp. 142–147, Jun. 2018.

[16] E. Barsoukov and J. Macdonald, *Impedance Spectroscopy Theory, Experiment, and Applications*, 2nd ed. Hoboken, NJ, USA: Wiley, 2005.

[17] A. Allagui, T. J. Freeborn, A. S. Elwakil, and B. J. Maundy, "Reevaluation of performance of electric double-layer capacitors from constant-current charge/discharge and cyclic voltammetry," *Sci. Rep.*, vol. 6, 2016, Art. no. 38568.

[18] J. Illig, *Physically Based Impedance Modelling of Lithium-Ion Cells*. Karlsruhe, Germany: KIT Scientific Publishing, 2014.

[19] C. Hamann, A. Hamnett, and W. Vielstich, *Electrochemistry*, 2nd ed. Weinheim, Germany: Wiley-VCH Verlag GmbH & Co., 2007.

[20] F. Huet, "A review of impedance measurements for determination of the state-of-charge or state-of-health of secondary batteries," *J. Power Sources*, vol. 70, no. 1, pp. 59–69, 1998.

[21] L. Juang, P. Kollmeyer, R. Zhao, T. Jahns, and R. Lorenz, "The impact of DC bias current on the modeling of lithium iron phosphate and lead-acid batteries observed using electrochemical impedance spectroscopy," in *Proc. IEEE Energy Convers. Congr. Expo.*, 2014, pp. 2575–2581.

[22] U. Westerhoff, K. Kurbach, F. Lienesch, and M. Kurrat, "Analysis of lithium-ion battery models based on electrochemical impedance spectroscopy," *Energy Technol.*, vol. 4, no. 12, pp. 1620–1630, Dec. 2016.

[23] S. Yuan, H. Wu, X. Zhang, and C. Yin, "Online estimation of electrochemical impedance spectra for lithium-ion batteries via discrete fractional order model," in *Proc. IEEE Vehicle Power Propulsion Conf.*, 2013, pp. 1–6.

[24] J. Song and M. Z. Bazant, "Effects of nanoparticle geometry and size distribution on diffusion impedance of battery electrodes," *J. Electrochemical Soc.*, vol. 160, no. 1, pp. A15–A24, May 2013.

[25] C. Mikolajczak, M. Kahn, K. White, and R. T. Long, *Lithium-Ion Batteries Hazard and Use Assessment*. New York, NY, USA: Springer-Verlag, 2011.

[26] H. Kang, "Geometric and electrochemical characteristics of lithium-ion batteries," M.S. Thesis, Purdue University, West Lafayette, IN, USA, 2017.

[27] V. Muenzel *et al.*, "Comment on a comparative testing study of commercial 18650-format lithium-ion battery cells," *J. Electrochemical Soc.*, vol. 162, no. 12, pp. Y11–Y12, Aug. 2015.

[28] F. C. Laman, M. W. Matsen, and J. A. R. Stiles, "Inductive impedance of a spirally wound Li/MoS_2 Cell," *J. Electrochemical Soc.*, vol. 133, no. 12, pp. 2441–2446, Dec. 1986.

[29] A. Senyshyn, M. J. Muhlbauer, O. Dolotko, M. Hofmann, and H. Ehrenberg, "Homogeneity of lithium distribution in cylinder-type li-ion batteries," *Sci. Rep.*, vol. 5, Dec. 2015, Art. no. 18380.

[30] C. L. Phillips and H. T. Nagle, *Digital Control System Analysis and Design*, 2nd ed. Upper Saddle River, NJ, USA: Prentice-Hall, 1990.

[31] A. J. Baurd and L. R. Faulkner, *Electrochemical Methods–Fundamental and Applications*, 2nd ed. New York, NY, USA: Wiley, 2001.

[32] T. Hang, D. Mukoyama, H. Nara, N. Takami, T. Momma, and T. Osaka, "Electrochemical impedance spectroscopy analysis for lithium-ion battery using $Li_4Ti_5O_{12}$ anode," *J. Power Sources*, vol. 222, pp. 442–447, Jan. 2013.

[33] D. I. Stroe, M. Swierczynski, A. I. Stan, V. Knap, R. Teodorescu, and S. J. Andreasen, "Diagnosis of lithium-ion batteries state-of-health based on electrochemical impedance spectroscopy technique," in *Proc. IEEE Energy Convers. Congr. Expo.*, 2014, pp. 4576–4582.

[34] V. Pop, H. J. Bergveld, D. Danilov, P. P. L. Regtien, and P. H. L. Notten, *Battery Management Systems—Accurate State-of-Charge Indication for Battery-Powered Applications*. London, UK: Springer—Phillips Research Book Services, 2008.

[35] K. Ng, C. Mo, Y. Chen, and Y. Hsieh, "State-of-charge estimation for lead-acid batteries based on dynamic open-circuit voltage," in *Proc. IEEE 2nd Int. Power Energy Conf.*, 2008, pp. 972–976.

[36] J. Christophersen, "Battery state-of-health assessment using a near real-time impedance measurement technique under no-load and load conditions," Ph.D. dissertation, Montana State University, Bozeman, Montana, USA, 2011.

[37] T. Stanciu, D. I. Stroe, R. Teodorescu, and M. Swierczynski, "Extensive EIS characterization of commercially available lithium polymer battery cell for performance modelling," in *Proc. IEEE 17th Eur. Conf. Power Electron. Appl.*, 2015, pp. 1–10.

[38] W. Press, B. Flannery, S. Teukolsky, and W. Vetterling, *Numerical Recipes in C: The Art of Scientific Computing*, 2nd ed. Cambridge, U.K., Cambridge Univ. Press, 1992.

[39] C. Cheng, H. Chung, and R. Lau, "Time-domain modeling of constant phase element for simulation of lithium batteries under arbitrary charging and discharging current profiles," in *Proc. IEEE Appl. Power Electron. Conf. Expo.*, 2017, pp. 985–992.

[40] M. Galeotti, L. Cina, C. Giammanco, S. Cordiner, and A. DiCarlo, "Performance analysis and SOH (state of health) evaluation of Lithium Polymer batteries through electrochemical impedance spectroscopy," *Energy*, vol. 89, pp. 678–686, Sep. 2015.

[41] G. Liu, K. H. Bai, and M. McAmmond, "Comparison of SiC MOSFETs and GaN HEMTs based high-efficiency high-power-density 7.2 kW EV battery chargers," in *Proc. IEEE 5th Workshop Wide Bandgap Power Devices Appl.*, 2017, pp. 391–397.

[42] J. Park, M. Kim, and S. Choi, "Fixed frequency series loaded resonant converter based battery charger which is insensitive to resonant component tolerances," in *Proc. 7th Int. Power Electron. Motion Control Conf.*, 2012, pp. 918–922.

[43] Y. Zhan, J. Zhu, Y. Guo, and H. Wang, "Development of a single-phase high frequency UPS with backup PEM fuel cell and battery," in *Proc. Int. Conf. Elect. Mach. Syst.*, 2007, pp. 1840–1844.

[44] C. Panchal and J. Lu, "High frequency planar transformer (HFPT) for universal contact-less battery charging platform," *IEEE Trans. Magn.*, vol. 47, no. 10, pp. 2764–2767, Oct. 2011.
[45] K. Rakhi, K. Ilango, H. V. Manjunath, and M. G. Nair, "Simulation analysis of half bridge series parallel resonant converter based battery charger for photovoltaic system," in *Proc. Power Energy Syst.: Towards Sustain. Energy*, 2014, pp. 1–5.
[46] F. Elwakil, A. Radwan, and A. Allagui, "Power and energy analysis of fractional-order electrical energy storage devices," *Energy*, vol. 111, pp. 785–792, 2016.
[47] T. Momma, M. Matsunaga, D. Mukoyama, and T. Osaka, "AC impedance analysis of Lithium ion battery under temperature control," *J. Power Sources*, vol. 216, no. 2, pp. 304–307, Jun. 2012.

Chun-Sing Cheng (S'16) received the B.Eng. degree in computer engineering (business intelligence minor) from the City University of Hong Kong, Kowloon, Hong Kong, in 2013, where he is currently working toward the M.Phil. degree in electronic engineering.

His current research interests include battery modeling and battery diagnosis.

Henry Shu-Hung Chung (M'95–SM'03–F'16) received the B.Eng. and the Ph.D. degrees in electrical engineering from the Hong Kong Polytechnic University, Kowloon, Hong Kong, in 1991 and 1994, respectively.

Since 1995, he has been with the City University of Hong Kong, Kowloon, Hong Kong, where he is currently a Professor with the Department of Electronic Engineering and the Director with the Center for Smart Energy Conversion and Utilization Research. He has edited one book, authored eight research book chapters, and over 400 technical papers including 180 refereed journal papers in his research areas, and holds 50 patents. His research interests include renewable energy conversion technologies, lighting technologies, smart-grid technologies, and computational intelligence for power electronic systems.

Dr. Chung was the recipient of numerous industrial awards for his invented energy saving technologies. He was the Chair of the Technical Committee of the High-Performance and Emerging Technologies, IEEE Power Electronics Society in 2010–2014. He is currently the Editor-in-Chief for the IEEE POWER ELECTRONICS LETTERS and the Associate Editor for the IEEE TRANSACTIONS ON POWER ELECTRONICS and the IEEE JOURNAL OF EMERGING AND SELECTED TOPICS IN POWER ELECTRONICS.

Ricky Wing-Hong Lau (M'88–SM'06) received the B.Sc. and Ph.D. degrees in electrical and electronic engineering from the University of Portsmouth, Portsmouth, U.K., in 1985 and 1989, respectively.

He joined the Department of Electronic Engineering, City University of Hong Kong, Kowloon, Hong Kong, in 1990 and is currently an Associate Professor there. His research interests include digital signal processing, digital audio engineering, pulsewidth modulation spectrum analysis, embedded system design, and smart-grid development.

Dr. Lau was the recipient of the IEEE Third Millennium Medal. He was the Chairman of the IEEE Hong Kong Section in 2005.

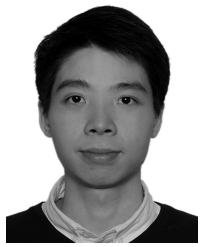

Kelvin Yi-Wen Hong received the B.Eng. degree in computer engineering from the City University of Hong Kong, Kowloon, Hong Kong, in 2015. He is currently working toward the Ph.D. degree in electronic engineering at the Department of Electronic Engineering, City University of Hong Kong.

His research interests include intelligent control and optimization of power electronic converters, fault diagnosis of power electronic systems, and machine learning.